Assignment 2

Group 11: Zhongwang Fu
Diwen Wang

1.Abstract

This study investigates wideband channel characterization and MIMO-based direction estimation. The first part examines the received power and amplitude distribution, analyzing impulse response behavior in relation to different bandwidth. Power-delay-profile (PDP) and root-mean-square (RMS) delay spread are also evaluated. The second part focuses on estimating the direction of arrival (DOA) using an 8 × 8 MIMO system. Conventional beamforming and Capon's minimum variance method (MVM) are applied for DOA estimation.

2.Introduction

This assignment contains 2 tasks. For task 1, we analyze the received power and amplitude distribution in an indoor wireless system. It also examines impulse response behavior and its relation to system bandwidth. Additionally, PDP, RMS delay spread, and time-frequency correlation will be studied. For task 2, the aim is to estimate the direction of departure and direction of arrival based on a measured 8 × 8 MIMO system. The measurement setup for each part will be stated in part3.

3.Methodology and Technical Results

3.1 Wideband characterization

3.1.1 Measurement setup and Method

The channel measurements are conducted using a vector network analyzer (VNA) connected to two broadband antennas. The network analyzer measures the transfer function, $H(t,f)$, at a number of frequency points. These antennas are mounted on rails with stepper motors, allowing them to move along a predefined path. The entire setup is controlled via LabView running on a laptop.

The transfer function is measured using the following settings:

- Frequency band: 5.4 − 5.6 GHz
- Frequency points: $N_f = 401$
- Number of positions along the linear rail: 91
- Antenna spacing along the linear rail: $\Delta d = 0.5\ cm$

3.1.2 Frequency transfer function $H(t,f)$

The 3D plot of $|H(t,f)|$ in dB is shown in figure 1. The fluctuations in $|H(t,f)|$ suggest constructive and destructive interference patterns, caused by multipath propagation due to reflections, diffractions, and scattering in the environment. The deep fades, where the amplitude drops significantly, correspond to destructive interference conditions where multipath components cancel each other out. Conversely, peaks represent constructive interference where multiple paths combine in-phase.

The numerous deep fades implies that the channel response follows a **Rayleigh** distribution, the model for **non-line-of-sight (NLOS) channels** dominated by multipath effects. A detailed statistical analysis of the measured $|H(t,f)|$ data will be conducted later to confirm the Rayleigh distribution assumption and further

characterize the fading properties of the channel.

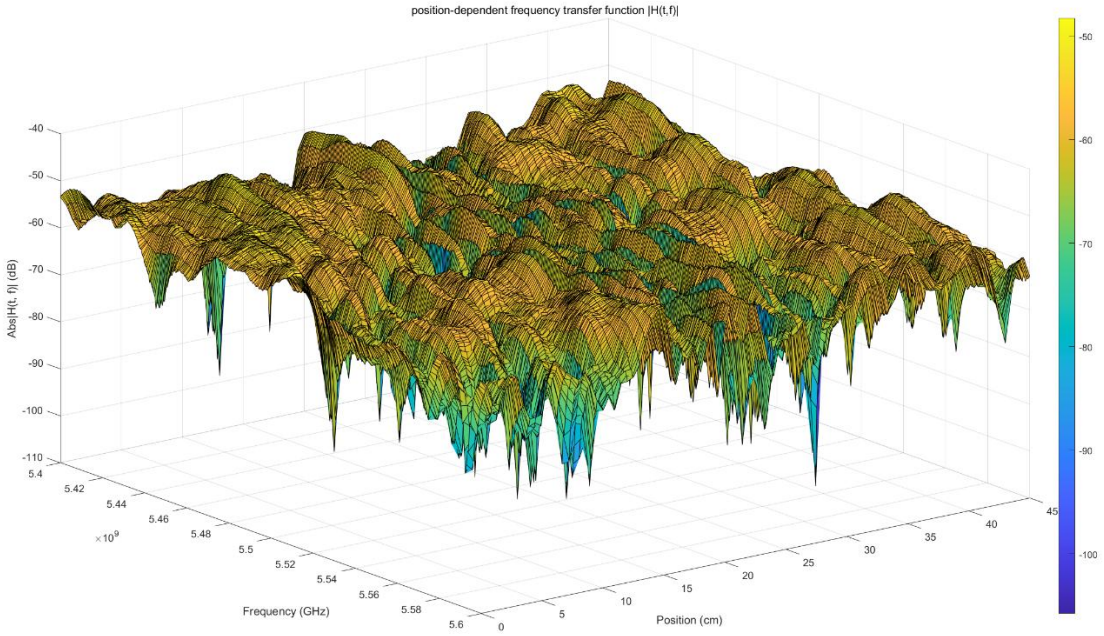

Fig.1 Position-dependent frequency transfer function $|\boldsymbol{H(t,f)}|$

3.1.3 Impulse response $\boldsymbol{h(t,\tau)}$

The impulse response $h(t,\tau)$ has been analyzed for three different bandwidths: full bandwidth (200 MHz), medium bandwidth (50 MHz), and small bandwidth (2.5 MHz). As shown in figures 2 to 4, the results demonstrate the significant impact of system bandwidth on the resolvability of multipath components in a wireless channel.

In the full-bandwidth case, the impulse response exhibits fine multipath resolvability, with distinct multipath components appearing as separate peaks in the delay axis. This high resolution is due to the wide bandwidth, which allows individual echoes to be distinguished based on their time delays. As the bandwidth decreases to the medium level, the impulse response becomes less detailed, with multipath components merging into broader peaks, reducing the ability to differentiate between closely spaced echoes.

In the small-bandwidth case, which satisfies the condition $W \ll \frac{1}{\tau_{max}}$, all echoes fall into a single delay bin, resulting in a smooth impulse response with minimal delay resolution.

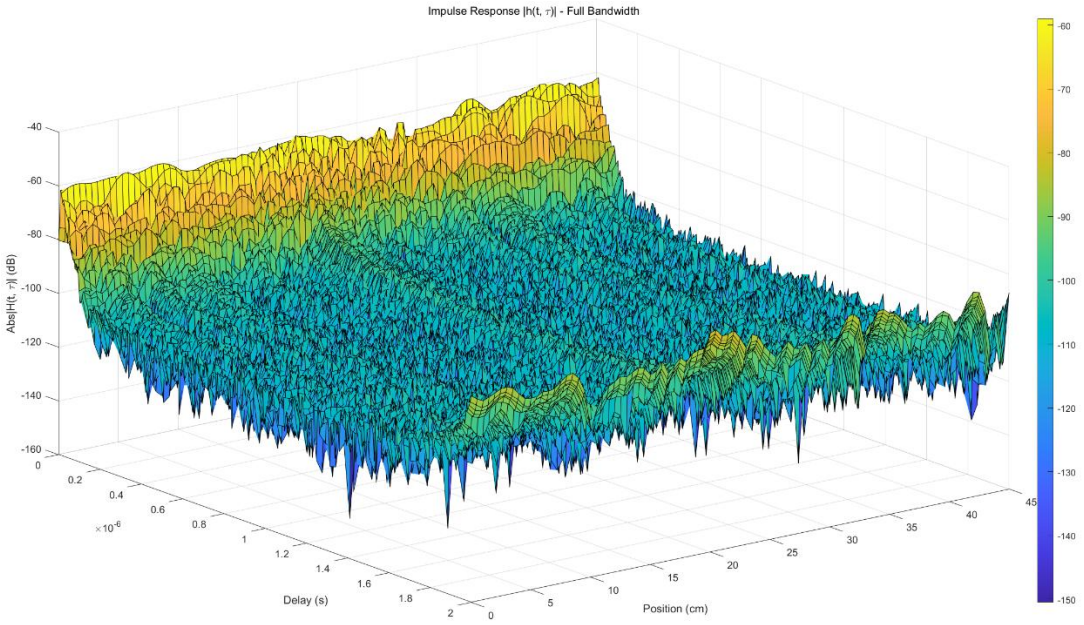

Fig.2 Impulse Response $|h(t,\tau)|$ - Full Bandwidth

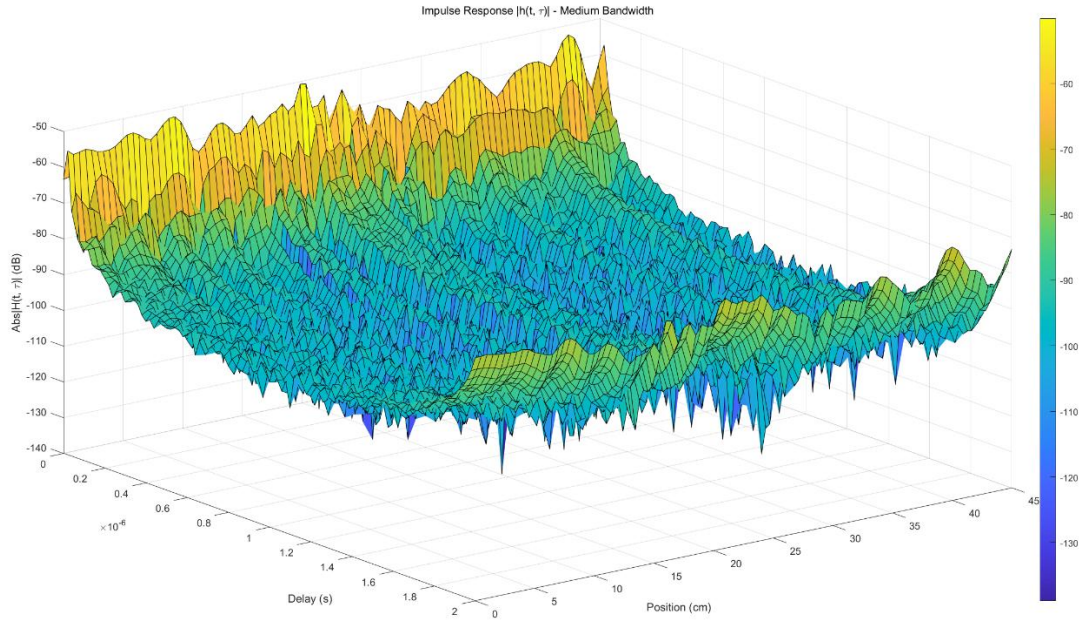

Fig.3 Impulse Response $|h(t,\tau)|$ - Medium Bandwidth

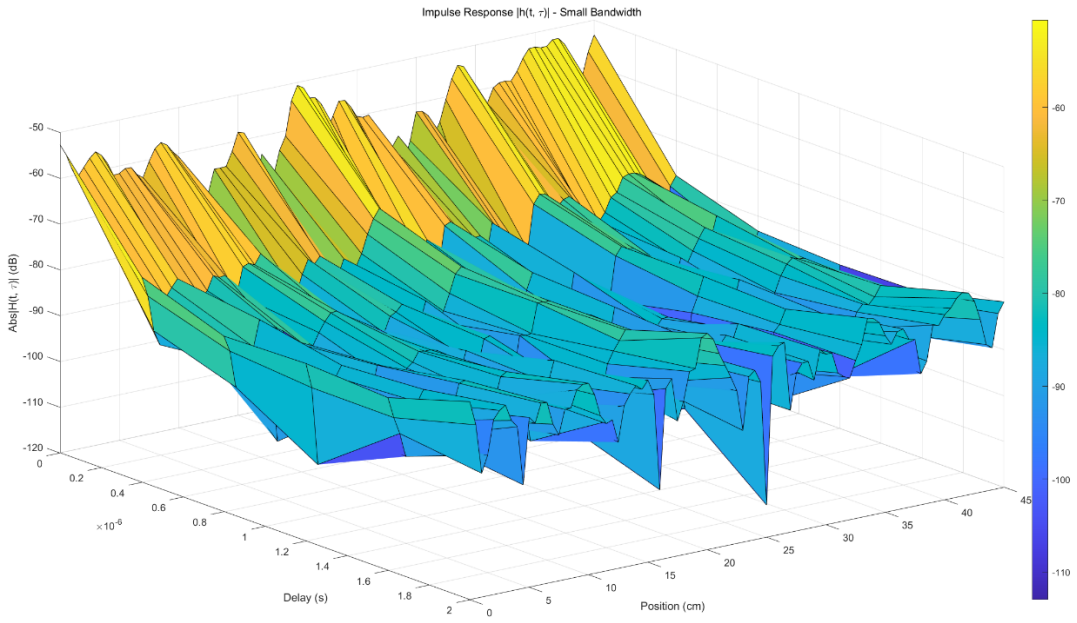

Fig.4 Impulse Response $|h(t,\tau)|$- Small Bandwidth

This behavior aligns with the mathematical characterization of narrowband and wideband systems: a system is classified as narrowband if the inverse of the system bandwidth $1/W$ is much larger than the maximum excess delay τ_{max}, causing all multipath components to collapse into a single bin, with the channel response represented by a single time-varying complex gain $\alpha(t)$. Conversely, in a wideband system, the multipath components are resolvable, and the received signal shape differs from the transmitted signal due to the time dispersion introduced by the channel [1].

3.1.4 Distribution of the Amplitude of the Frequency Transfer Function

By plotting both the Probability Density Function (PDF) and the Cumulative Distribution Function (CDF), we can investigate how the amplitude of $|H(t,f)|$ is statistically distributed.

From the PDF plot shown in figure 5, it is evident that the empirical distribution closely follows a **Rayleigh distribution**, which indicates that the channel is **Non-Line-of-Sight (NLOS) channel**. To validate this observation, theoretical Rayleigh and

Rician distributions were overlaid on the empirical PDF. The resulting fit shows that the Rayleigh and Rician theoretical curves are nearly identical, which mathematically confirms that when the Rician factor $K_r = 0$, the Rician distribution simplifies to a Rayleigh distribution. This suggests that the observed channel is a **non-line-of-sight (NLOS)** environment, where the received signal is composed of numerous scattered multipath components rather than a strong direct path.

The CDF shown in figure 6 further supports this conclusion, as the empirical CDF aligns well with both the theoretical Rayleigh and Rician CDF curves. The strong agreement between empirical and theoretical distributions demonstrates that the frequency transfer function's amplitude distribution is well-characterized by Rayleigh statistics.

In summary, the observed results indicate that the wireless channel under study exhibits rich multipath propagation, where the amplitude of the received signal follows the Rayleigh distribution due to the absence of a strong dominant path component.

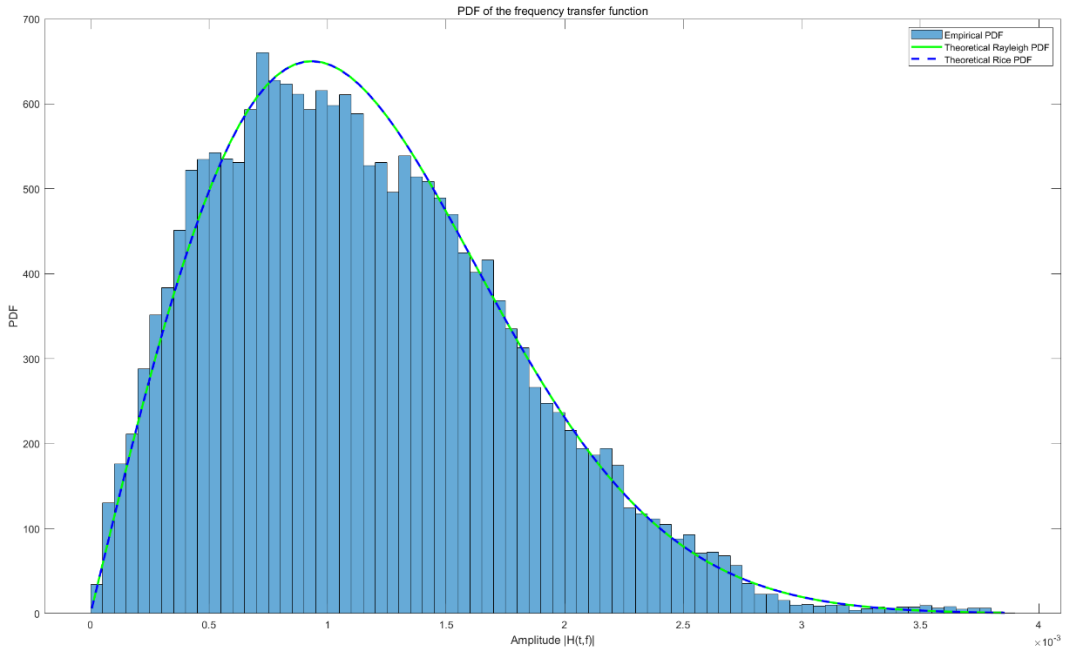

Fig.5 Empirical and Theoretical Rayleigh and Rice PDF of frequency transfer function

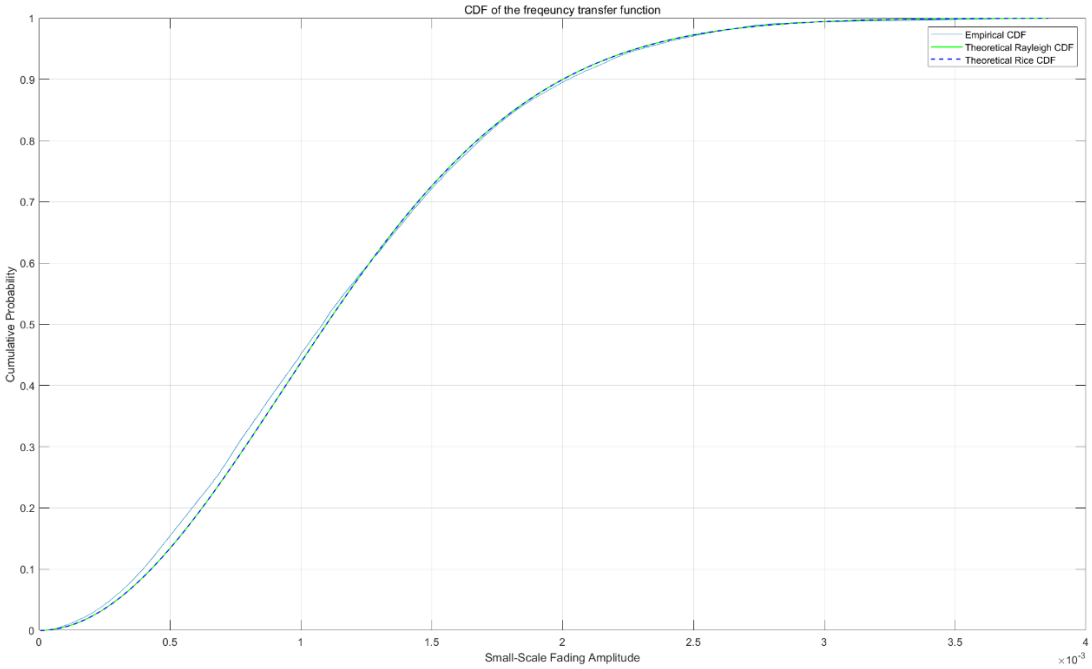

Fig.6 Empirical and Theoretical Rayleigh and Rice CDF of frequency transfer function

3.1.5 Distribution of the Amplitude for Different Taps of the Impulse Response

The visualization of the taps of the impulse response, where the impulse response is binned into discrete delay intervals of width $\Delta\tau = 5ns$ is shown in figure 7. The fundamental observation from this bar is that in a realistic environment, Interaction Objects (IOs) do not align perfectly on a single ellipse corresponding to a fixed delay. Instead, reflections arrive over a range of delays, making the channel inherently dispersive. The extent to which this dispersion impacts the system behavior depends on the bandwidth W of the receiver. A receiver with finite bandwidth cannot resolve delays smaller than $\frac{1}{W}$, meaning that multipath components (MPCs) arriving within a time window $\Delta\tau$ are indistinguishable and contribute to the same effective delay bin.

If enough nondominant IOs are in each donut-shaped region, then the MPCs falling into each delay bin fulfill the central limit theorem. In that case, the amplitude of each bin can be described statistically, and the probability density function (pdf) of this amplitude is Rayleigh. The minimum delay in the plot corresponds to the direct

Line-of-Sight (LOS) component, traveling at the speed of light c_0, while the maximum delay represents the longest significant reflection path that still contributes measurably to the impulse response. The difference between these two values defines the maximum excess delay τ_{max}, which is crucial for characterizing the coherence bandwidth of the channel [1].

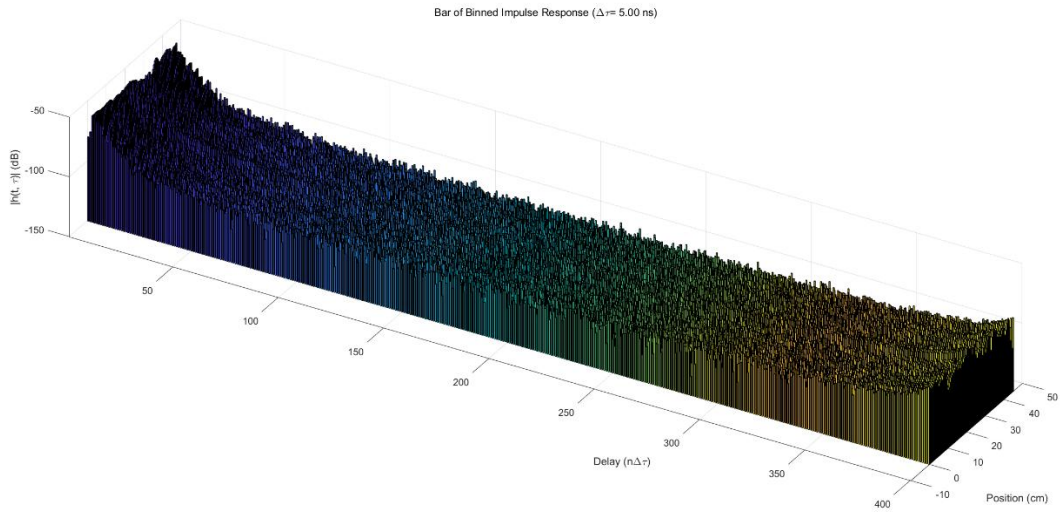

Fig.7 Bar of Binned Impulse Response ($\Delta\tau = 5ns$)

Then we investigated the distribution of the amplitude of the impulse response at different delay bins, specifically at the beginning, middle and end.

From the PDF and CDF plots shown in figures 8 and 9, we can see that **at the beginning**, the distribution appears to follow either a Normal or Rice distribution, but it is difficult to distinguish between them visually. To determine the best-fitting distribution, we conducted a Kolmogorov-Smirnov (KS) test against Normal, Rayleigh, and Rice distributions. The KS test result for the normal distribution is $p = 0.970555$, for the Rayleigh distribution, the result is $p = 0.241837$ and for the Rice distribution, the test result is $p = 0.936208$. These results confirm that at the beginning of the impulse response, the amplitude distribution follows a **Normal distribution** more closely than a Rayleigh or Rice distribution.

The reason for this statistical behavior can be attributed to the nature of multipath propagation at different time instances. At the beginning of the impulse response, the signal primarily consists of the earliest-arriving multipath components, which may include a direct Line-of-Sight (LOS) path and strong early reflections from large

surfaces such as walls or the ground. The reason for this statistical behavior is primarily related to large-scale fading effects, specifically path loss and shadowing, which dominate the received signal characteristics at the beginning of the impulse response.

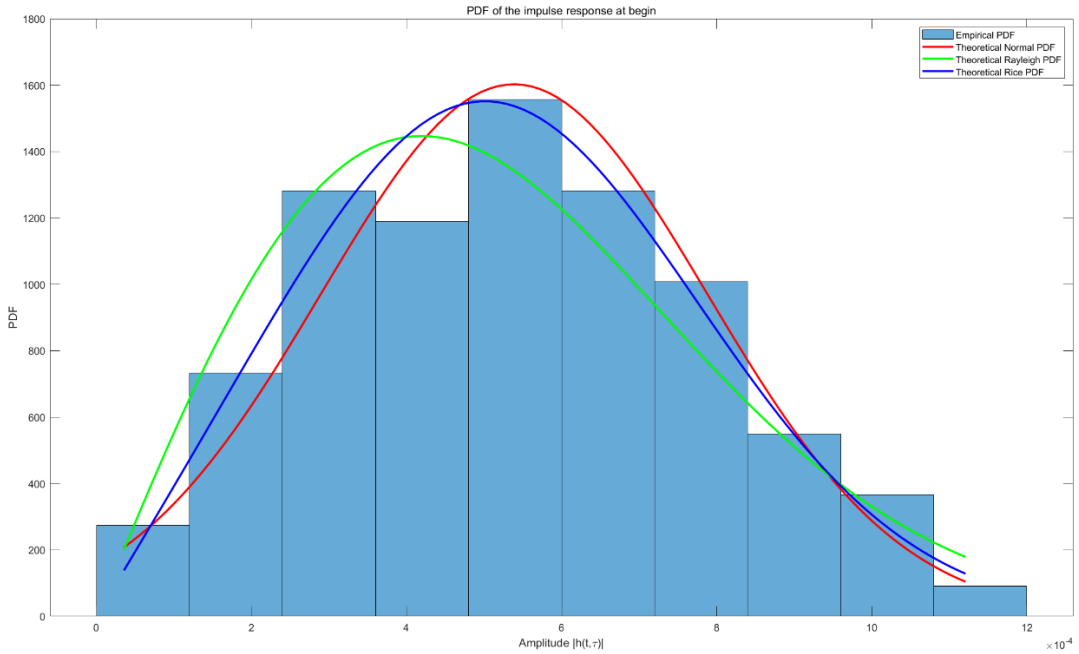

Fig.8 Empirical and Theoretical Normal, Rayleigh and Rice PDF of impulse response at begin

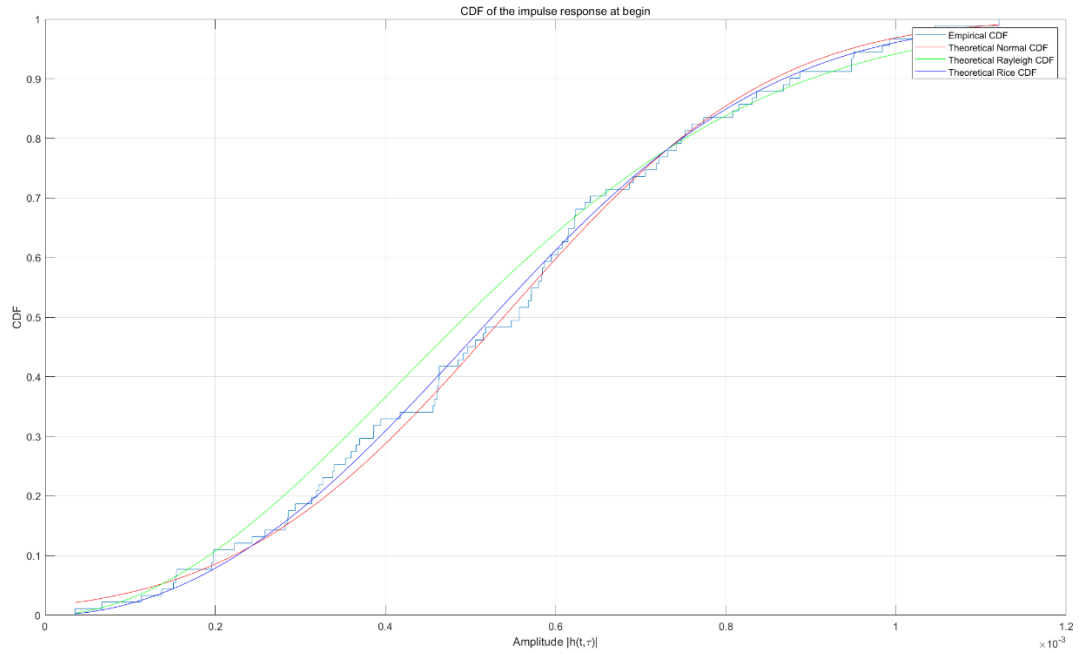

Fig.9 Empirical and Theoretical Normal, Rayleigh and Rice CDF of impulse response at begin

When examining the **middle and end bins**, the amplitude distribution aligns more closely with the Rayleigh distribution. From the PDF and CDF plots for the middle bins

shown in figures 10 and 11, it is evident that the empirical distribution closely follows the Rayleigh theoretical curve. At the end bins, as is shown in figures 12 and 13, the amplitude distribution still follows a **Rayleigh distribution**. The theoretical Rician and Rayleigh fitting curves are identical. This is because, when the Rician factor $K_r = 0$, the Rician distribution reduces to a Rayleigh distribution, meaning there is no dominant LOS component in this region.

Initially, the amplitude variations are dominated by large-scale effects, such as distance-dependent path loss, leading to a normal distribution. As the impulse response progresses, small-scale fading effects become dominant, and the received signal is composed of many scattered multipath components, resulting in a Rayleigh distribution. The fact that the Rician and Rayleigh fits coincide at the end confirms the absence of a significant LOS path, further validating the assumption that the environment is rich in multipath scattering.

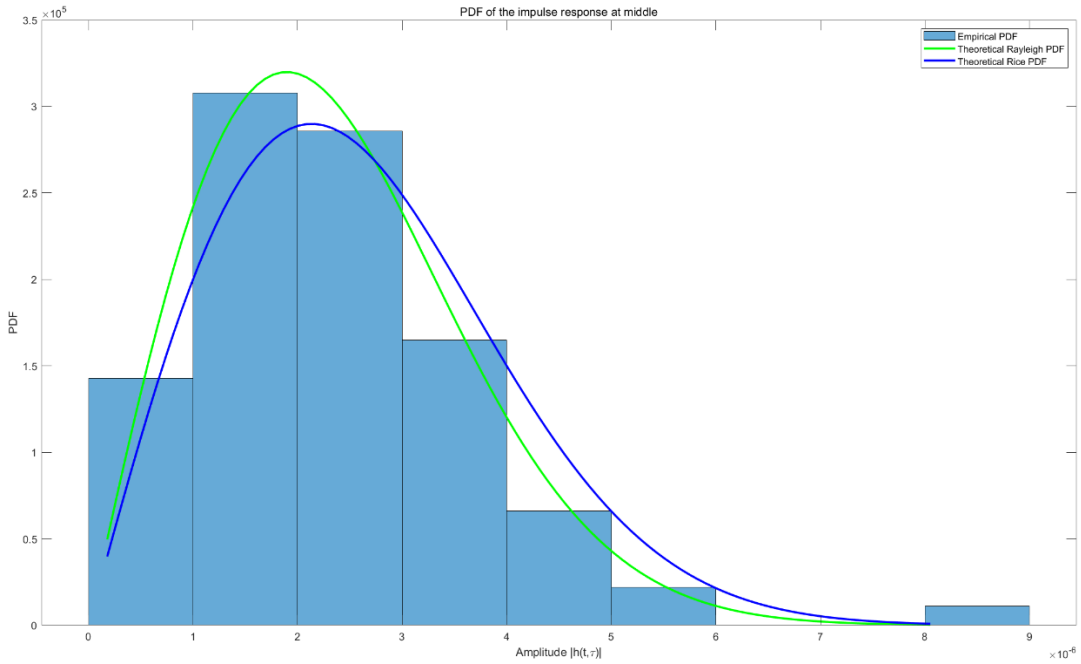

Fig.10 Empirical and Theoretical Rayleigh and Rice PDF of impulse response at middle

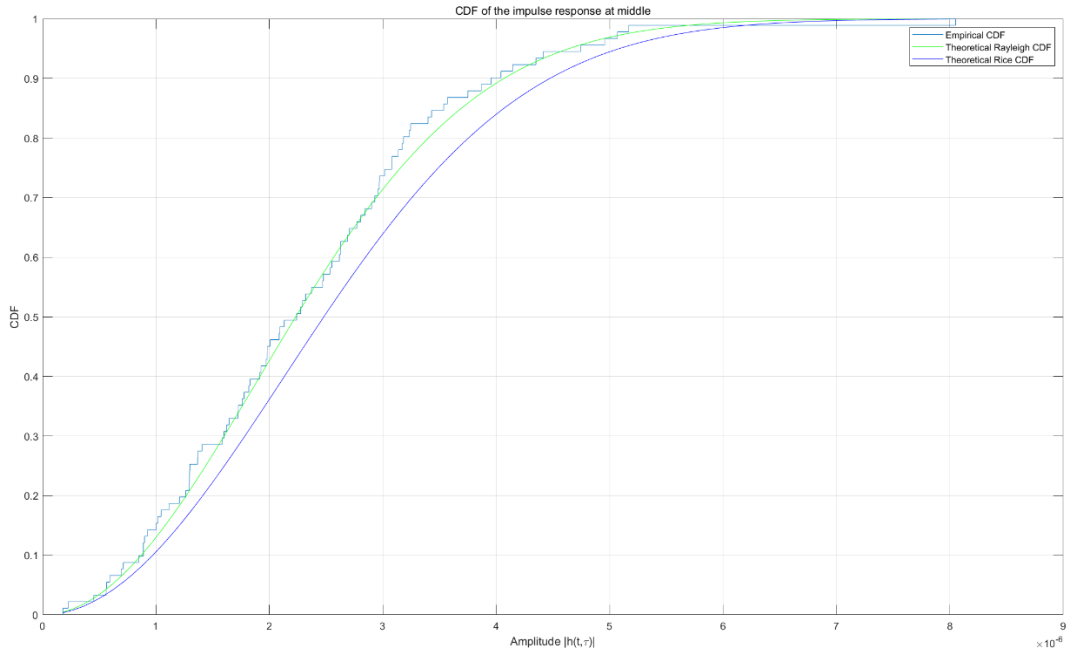

Fig.11 Empirical and Theoretical Rayleigh and Rice CDF of impulse response at middle

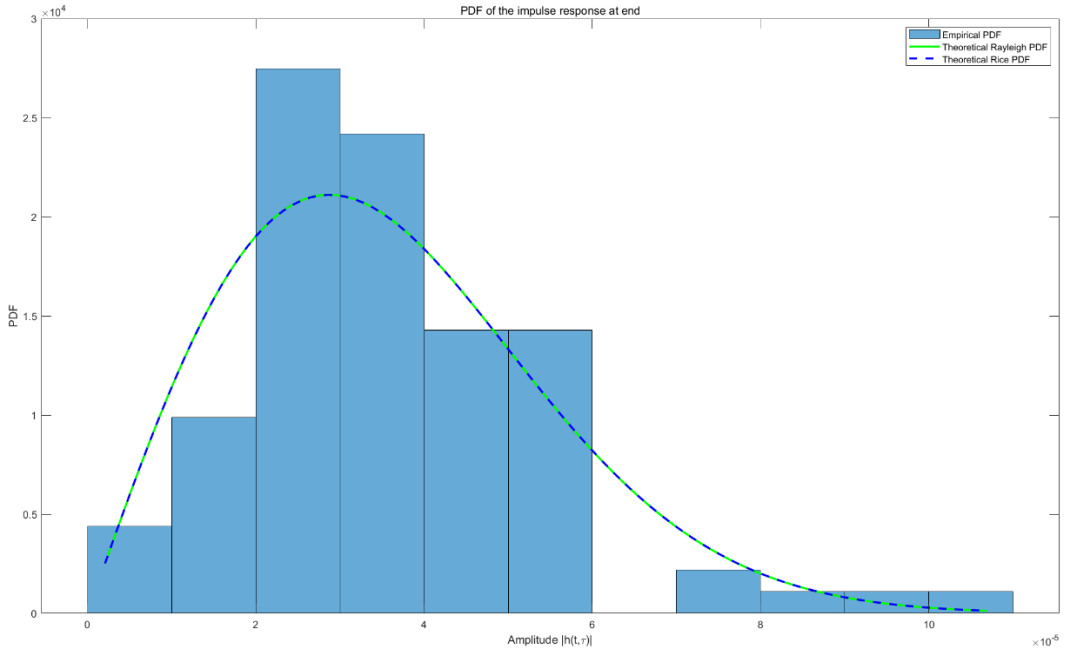

Fig.12 Empirical and Theoretical Rayleigh and Rice PDF of impulse response at end

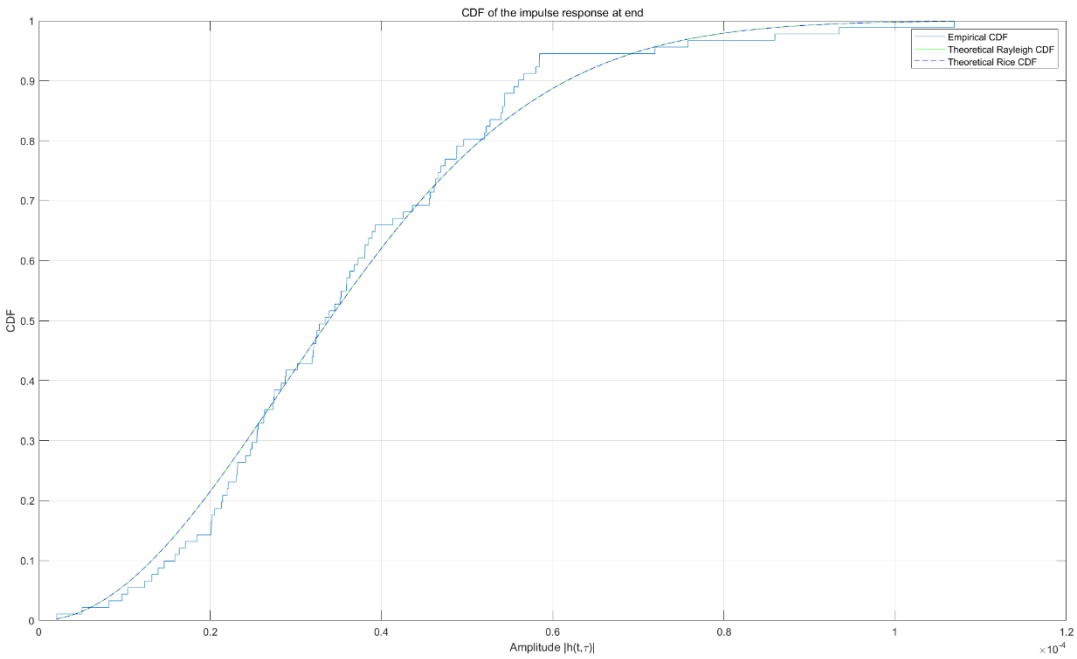

Fig.13 Empirical and Theoretical Rayleigh and Rice CDF of impulse response at end

3.1.6 PDP and the RMS delay spread

The PDP contains information about how much power (from a transmitted delta pulse with unit energy) arrives at the RX with a delay between $(\tau, \tau + d\tau)$, irrespective of a possible Doppler shift. The PDP can be obtained from the complex impulse responses $h(t, \tau)$ as [1]:

$$P_h(\tau) = \lim_{T \to \infty} \frac{1}{2T} \int_{-T}^{T} |h(t, \tau)|^2 dt \quad (1)$$

The measured PDP is shown in figure 14, illustrating the power distribution over time delays.

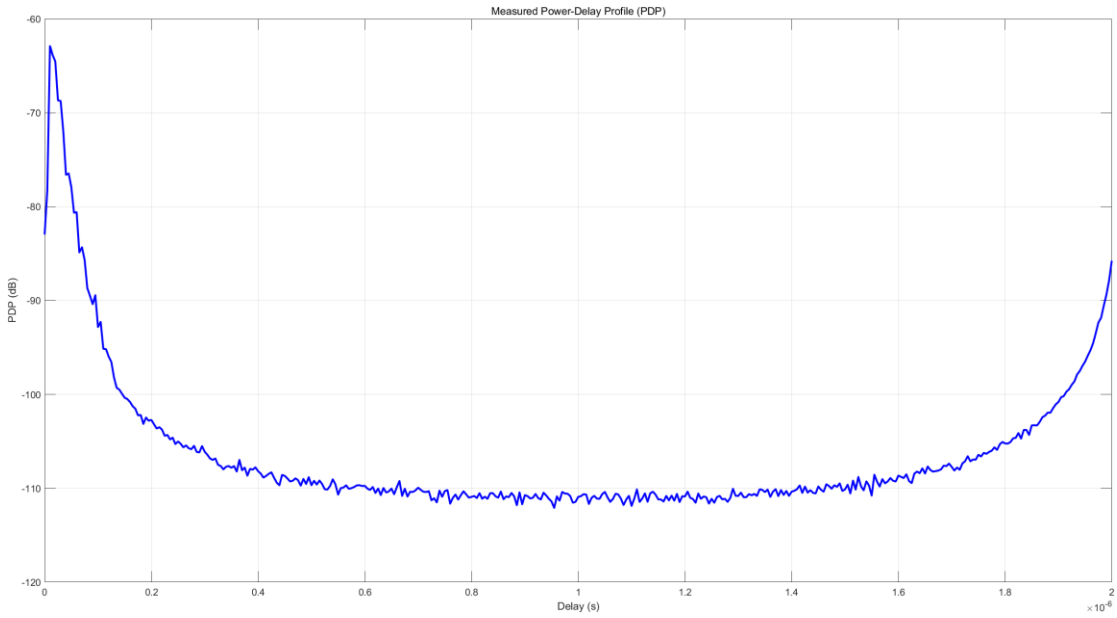

Fig.14 Measured Power-Delay Profile (PDP)

The PDP is a function, but for obtaining a quick overview of measurement results, it is preferable to have each measurement campaign described by a single parameter. While there are a large number of possible parameters, normalized moments of the PDP are the most popular [1].

We start out by computing the zeroth-order moment – i.e., delay-integrated power:

$$P_m = \int_{-\infty}^{\infty} P_h(\tau) d\tau \tag{2}$$

The normalized first-order moment, the mean delay is given by:

$$T_{\mathrm{m}} = \frac{\int_{-\infty}^{\infty} P_{\mathrm{h}}(\tau)\tau d\tau}{P_{\mathrm{m}}} \tag{3}$$

The square root of the normalized second-order central moment is known as rms delay spread and is defined as:

$$S_\tau = \sqrt{\frac{\int_{-\infty}^{\infty} P_{\mathrm{h}}(\tau)\tau^2 d\tau}{P_{\mathrm{m}}} - T_{\mathrm{m}}^2} \tag{3}$$

The rms delay spread has obtained a special stature among all parameters. From our measured PDP, we obtained the following results:

Mean delay: $T_m = 34.15ns$

RMS delay spread: $S_\tau = 165.76ns$

3.2 MIMO and Directional Aspects

3.2.1 Measurement setup and Method

This measurement setup is for an 8 × 8 MIMO system with uniform linear arrays (ULA). The goal is now to estimate the direction of arrival (DOA) of the LOS component. The basic measurement setup is shown in figure 15.

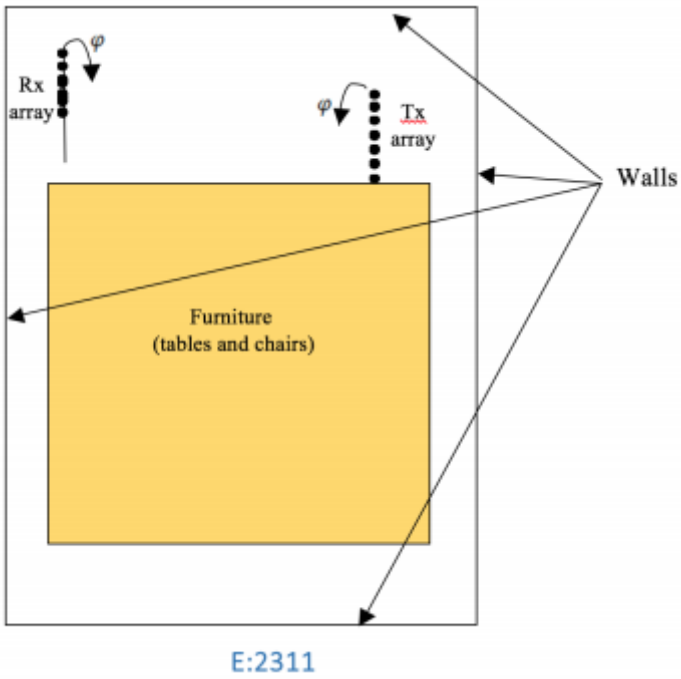

Fig. 15 Measurement setup for the 8 × 8 MIMO case

The transfer function is measured using the following settings on the VNA:

- Frequency band: 5.1 − 5.3 GHz
- Frequency points: $N_f = 201$
- Number of (virtual) Tx elements: 8
- Number of (virtual) Rx elements: 8
- Antenna spacing for the uniform linear arrays (same at Tx and Rx): $\Delta d = \lambda/2$

3.2.2 Results

The measured signal can be modeled as:

$$y = Hx + n \tag{4}$$

where y is the received signal, x is the transmitted signal and n is a noise vector. The correlation matrix describing the signal at Rx array for the direction of arrival DOA is given by

$$R_{rr} = E[r(t)r^H(t)] \tag{5}$$

where $r(t)$ is the array response, i.e., the received signal at all the antenna elements.

The beam-steering vector is a function of the direction of arrival, θ, and is given by

$$a(\theta) = \left[1\ e^{-j\frac{2\pi}{\lambda}\Delta dcos(\theta)}\ \ e^{-j2\frac{2\pi}{\lambda}\Delta dcos(\theta)}\ \ldots\ \ e^{-j7\frac{2\pi}{\lambda}\Delta dcos(\theta)}\right]^T \tag{6}$$

The angular spectrum for the conventional beamformer is given by:

$$P_{BF}(\theta) = \frac{a^H(\theta)R_{rr}a(\theta)}{a(\theta)^H a(\theta)} \tag{7}$$

The Minimum Variance Method (MVM) beamformer is given by

$$P_{BF}(\theta) = \frac{1}{a^H(\theta)R_{rr}^{-1}a(\theta)} \tag{8}$$

The final results are illustrated in the figure 16, where the conventional beamforming (BF) method produces peaks at $\boldsymbol{\theta = 104.5°}$ **and** $\boldsymbol{61.5°}$, indicating the estimated DOAs with limited resolution. In contrast, the MVM beamformer achieves a higher resolution, successfully identifying additional peaks at $\boldsymbol{98.5°, 108°, 56.5°}$ **and** $\boldsymbol{66°}$, demonstrating its superior ability to resolve closely spaced multipath components or sources. However, it can be seen that it is required that the correlation matrix does not become singular. Such singular R_{rr} typically occurs if the sources of the waves from the different directions are correlated. For channel sounding, all signals typically come from the same source, so that they are completely correlated. In that case, subarray averaging has to be used to obtain the correct correlation matrix. The drawback of subarray averaging is that it decreases the effective size of the array [1].

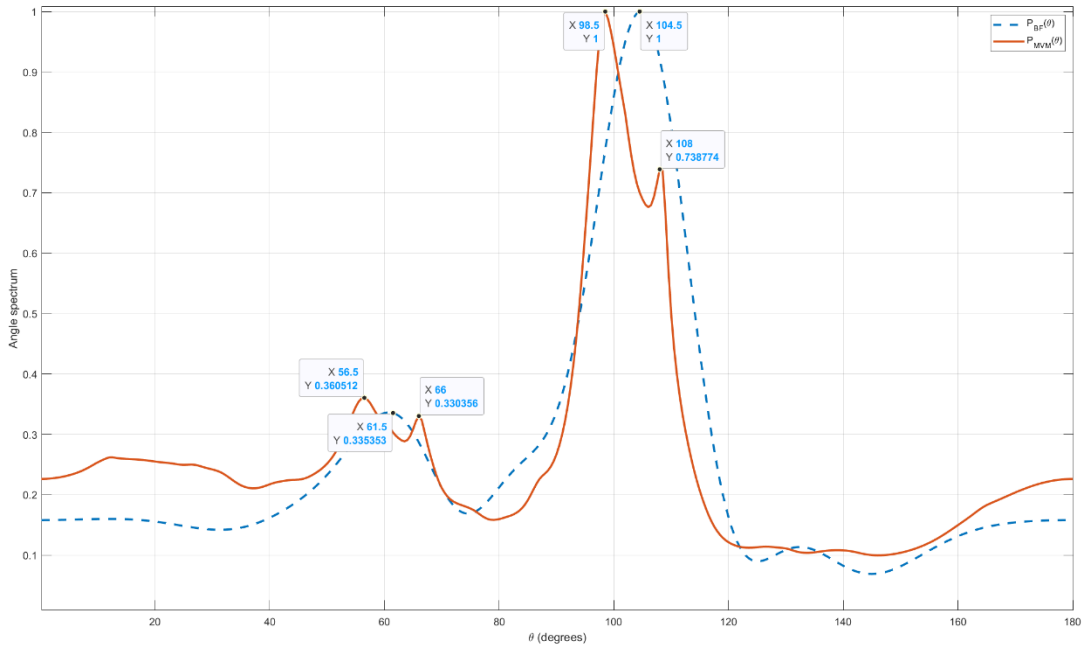

Fig. 16 Results of Angular Spectra for Conventional and MVM Beamformers

4. Conclusions

This study provided a detailed characterization of a wideband wireless channel and investigated Direction of Arrival (DOA) estimation using an 8 × 8 MIMO system.

In the first part, we analyzed the frequency transfer function $H(t, f)$ and impulse response $h(t, \tau)$, observing the effects of bandwidth on multipath resolvability. The Power Delay Profile (PDP) and RMS delay spread were evaluated to quantify the time dispersion of the channel. The results showed that a wider bandwidth enables finer resolution of multipath components, while a narrow bandwidth limits the delay resolution. The statistical analysis of the frequency transfer function amplitude confirmed that the channel exhibits Rayleigh fading, indicative of a Non-Line-of-Sight (NLOS) environment with rich multipath scattering. The impulse response amplitude was also examined at different delay bins, showing a transition from a Normal distribution at the beginning (due to large-scale fading effects) to a Rayleigh distribution in the later bins (due to small-scale multipath fading).

In the second part, we focused on DOA estimation using conventional

beamforming (BF) and Capon's Minimum Variance Method (MVM). The results demonstrated that BF provides a limited resolution, producing peaks at $\theta = 104.5°$ and $61.5°$, whereas MVM achieves a higher resolution, resolving additional peaks at $98.5°, 108°, 56.5°$ and $66°$. This highlights the superior ability of MVM to distinguish closely spaced multipath components, making it more suitable for scenarios with dense multipath propagation.

5. Reference

[1] Molisch, Andreas F. Wireless communications: from fundamentals to beyond 5G. John Wiley & Sons, 2022.

6. Appendix

6.1 Wideband characterization

```
clear; %Clear all variables in the workspace
close all; %Closes all figure windows
clc %Clear command window

%Load the data for Assignment 2
load('Hcorrected.mat');

Nt = 91;
Nf = 401;
frequencies = linspace(5.4e9, 5.6e9, Nf);
positions = (0:Nt - 1) * 0.5;
H_abs = abs(Hcorrected);

% T1.1
```

```
% H(t, f)
[P, F] = meshgrid(positions, frequencies);
figure(1);
surf(P, F, 20*log10(H_abs)');
xlabel('Position (cm)');
ylabel('Frequency (GHz)');
zlabel('Abs|H(t, f)| (dB)');
title('position-dependent frequency transfer function |H(t,f)|');
set(gca, 'YDir', 'reverse');
colorbar;

% T1.2
% h(t, \tau)
% Full bandwidth
B_full = frequencies(end) - frequencies(1);
taus_full = (0:Nf - 1) * (1 / B_full);
h_full = ifft(Hcorrected, [], 2);

[P_full, Tau_full] = meshgrid(positions, taus_full);
figure(2);
surf(P_full, Tau_full, 20*log10(abs(h_full))');
xlabel('Position (cm)');
ylabel('Delay (s)');
zlabel('Abs|H(t, \tau)| (dB)');
title('Impulse Response |h(t, \tau)| - Full Bandwidth');
set(gca, 'YDir', 'reverse');
colorbar;

% Medium bandwidth
Nf_med = 101;
```

```
B_med = frequencies(Nf_med) - frequencies(1);
taus_med = (0:Nf_med - 1) * (1 / B_med);
H_med = Hcorrected(:, 1:Nf_med);
h_med = ifft(H_med, [], 2);

[P_med, Tau_med] = meshgrid(positions, taus_med);
figure(3);
surf(P_med, Tau_med, 20*log10(abs(h_med))');
xlabel('Position (cm)');
ylabel('Delay (s)');
zlabel('Abs|H(t, \tau)| (dB)');
title('Impulse Response |h(t, \tau)| - Medium Bandwidth');
set(gca, 'YDir', 'reverse');
colorbar;

% Small bandwidth
% 1/B >> \Delta \tau_{max}
Nf_small = 6;
B_small = frequencies(Nf_small) - frequencies(1);
taus_small = (0:Nf_small - 1) * (1 / B_small);
H_small = Hcorrected(:, 1:Nf_small);
h_small = ifft(H_small, [], 2);

[P_small, Tau_small] = meshgrid(positions, taus_small);
figure(4);
surf(P_small, Tau_small, 20*log10(abs(h_small))');
xlabel('Position (cm)');
ylabel('Delay (s)');
zlabel('Abs|H(t, \tau)| (dB)');
title('Impulse Response |h(t, \tau)| - Small Bandwidth');
```

```
set(gca, 'YDir', 'reverse');
colorbar;
grid on;

% T1.3
% Investigate the distribution of the amplitude of the frequency transfer function.
H_flat = H_abs(:);

figure(5);

histogram(H_flat, 'Normalization', 'pdf');

hold on;
x_H = linspace(min(H_flat), max(H_flat));

rayleigh_fit = fitdist(H_flat, 'Rayleigh');
rayleigh_pdf = pdf(rayleigh_fit, x_H);

rician_fit = fitdist(H_flat, 'Rician');
rician_pdf = pdf(rician_fit, x_H);

plot(x_H, rayleigh_pdf, 'g', 'LineWidth', 2);
plot(x_H, rician_pdf, 'b--', 'LineWidth', 2);

xlabel('Amplitude |H(t,f)|');
ylabel('PDF');
title('PDF of the frequency transfer function');
legend('Empirical PDF', 'Theoretical Rayleigh PDF', 'Theoretical Rice PDF');

% CDF of frequency transfer function
```

```
figure(6);

cdfplot(H_flat);
hold on;

hat_sigma2_R = 1 / (2 * length(H_flat)) * sum(H_flat.^2);
x_H_cdf = linspace(min(H_flat), max(H_flat), length(H_flat));
rayleigh_CDF = 1 - exp(-x_H_cdf.^2/(2 * hat_sigma2_R));

rician_fit = fitdist(H_flat, 'Rician');
sigma_Rice = rician_fit.sigma;
upsilon_Rice = rician_fit.s;

rician_CDF_H = 1 - marcumq(upsilon_Rice/sigma_Rice, x_H_cdf/sigma_Rice);

plot(x_H_cdf, rayleigh_CDF, 'g', 'Linewidth', 1);
plot(x_H_cdf, rician_CDF_H, 'b--', 'Linewidth', 1);

xlabel('Small-Scale Fading Amplitude');
ylabel('Cumulative Probability');
legend('Empirical CDF', 'Theoretical Rayleigh CDF', 'Theoretical Rice CDF');
title('CDF of the frequency transfer function');
grid on;

% T1.4
h_amp = abs(h_full);
Delta_tau = 5 * 1e-9;
N_tau = floor(max(taus_full)/Delta_tau);

h_amp_binned = zeros(size(h_amp, 1), N_tau);
```

```
    for i = 1:N_tau
        start_idx = round((i - 1)*(Delta_tau / (taus_full(2) - taus_full(1)))) + 1;
        end_idx = start_idx + round(Delta_tau/(taus_full(2) - taus_full(1))) - 1;

        h_amp_binned(:, i) = mean(h_amp(:, start_idx:end_idx), 2);
    end

    figure(7);
    h_amp_binned_dB = 20 * log10(h_amp_binned);
    h_bar = bar3(positions, h_amp_binned_dB, 0.5);
    xlabel('Delay (n\Delta\tau)');
    ylabel('Position (cm)');
    zlabel('|h(t, \tau)| (dB)');
    title(sprintf('Bar of Binned Impulse Response (\\Delta\\tau= %.2f ns)',
Delta_tau*1e9));
    set(gca, 'YDir', 'normal');

    z_min = min(h_amp_binned_dB(:));
    for k = 1:length(h_bar)
        ZData = h_bar(k).ZData;
        ZData(ZData == 0) = z_min;
        h_bar(k).ZData = ZData;
    end
    view(30, 30)
    grid on;

    % Investigate the distribution of the amplitude for different taps of the impulse
response
```

```
% PDF of begin
h_amp_begin = h_amp_binned(:, 5);
figure(8);
histogram(h_amp_begin, 'Normalization', 'pdf', 'NumBins', 10);

hold on;
x_h = linspace(min(h_amp_begin), max(h_amp_begin));
normal_fit = fitdist(h_amp_begin, 'Normal');
normal_pdf = pdf(normal_fit, x_h);

rayleigh_fit = fitdist(h_amp_begin, 'Rayleigh');
rayleigh_pdf = pdf(rayleigh_fit, x_h);

rician_fit = fitdist(h_amp_begin, 'Rician');
rician_pdf = pdf(rician_fit, x_h);

plot(x_h, normal_pdf, 'r', 'LineWidth', 2);
plot(x_h, rayleigh_pdf, 'g', 'LineWidth', 2);
plot(x_h, rician_pdf, 'b', 'LineWidth', 2);

xlabel('Amplitude |h(t,\tau)|');
ylabel('PDF');
legend('Empirical PDF', 'Theoretical Normal PDF', 'Theoretical Rayleigh PDF',
'Theoretical Rice PDF');
title('PDF of the impulse response at begin');

% PDF of middle
middle_idx = floor(size(h_amp_binned, 2)) / 2;
h_amp_middle = h_amp_binned(:, middle_idx);
figure(9);
```

```
histogram(h_amp_middle, 'Normalization', 'pdf');

hold on;
x_h_mid = linspace(min(h_amp_middle), max(h_amp_middle));
rayleigh_fit_mid = fitdist(h_amp_middle, 'Rayleigh');
rayleigh_pdf_mid = pdf(rayleigh_fit_mid, x_h_mid);

rician_fit_mid = fitdist(h_amp_middle, 'Rician');
rician_pdf_mid = pdf(rician_fit_mid, x_h_mid);

plot(x_h_mid, rayleigh_pdf_mid, 'g', 'LineWidth', 2);
plot(x_h_mid, rician_pdf_mid, 'b', 'LineWidth', 2);

xlabel('Amplitude |h(t,\tau)|');
ylabel('PDF');
legend('Empirical PDF', 'Theoretical Rayleigh PDF', 'Theoretical Rice PDF');
title('PDF of the impulse response at middle');

% PDF of end
h_amp_end = h_amp_binned(:, size(h_amp_binned, 2));
figure(10);
histogram(h_amp_end, 'Normalization', 'pdf');
hold on;

x_h_end = linspace(min(h_amp_end), max(h_amp_end));
rayleigh_fit_end = fitdist(h_amp_end, 'Rayleigh');
rayleigh_pdf_end = pdf(rayleigh_fit_end, x_h_end);

rician_fit_end = fitdist(h_amp_end, 'Rician');
rician_pdf_end = pdf(rician_fit_end, x_h_end);
```

```
plot(x_h_end, rayleigh_pdf_end, 'g', 'LineWidth', 2);
plot(x_h_end, rician_pdf_end, 'b--', 'LineWidth', 2);

xlabel('Amplitude |h(t,\tau)|');
ylabel('PDF');
legend('Empirical PDF', 'Theoretical Rayleigh PDF', 'Theoretical Rice PDF');
title('PDF of the impulse response at end');

% CDF of begin
figure(11);
cdfplot(h_amp_begin);
hold on;
x_h_cdf = linspace(min(h_amp_begin), max(h_amp_begin),
length(h_amp_begin));
mu_LSF_h = mean(h_amp_begin);
sigma_LSF_h = std(h_amp_begin, 1);
normal_CDF_h = 0.5 * (1 + erf((x_h_cdf - mu_LSF_h)/(sigma_LSF_h *
sqrt(2))));

hat_sigma2_R_begin = 1 / (2 * length(h_amp_begin)) * sum(h_amp_begin.^2);
rayleigh_CDF_h_begin = 1 - exp(-x_h_cdf.^2/(2 * hat_sigma2_R_begin));

rician_fit = fitdist(h_amp_begin, 'Rician');
sigma_Rice = rician_fit.sigma;
upsilon_Rice = rician_fit.s;

rician_CDF_h_begin = 1 - marcumq(upsilon_Rice/sigma_Rice,
x_h_cdf/sigma_Rice);
```

```
plot(x_h_cdf, normal_CDF_h, 'r-');
plot(x_h_cdf, rayleigh_CDF_h_begin, 'g-');
plot(x_h_cdf, rician_CDF_h_begin, 'b-');

xlabel('Amplitude |h(t,\tau)|');
ylabel('CDF');
legend('Empirical CDF', 'Theoretical Normal CDF', 'Theoretical Rayleigh CDF', 'Theoretical Rice CDF');
title('CDF of the impulse response at begin');

[h_KS_LSF_Norm, p_KS_LSF_Norm, KSstat_LSF_Norm, cv_KS_LSF_Norm] = kstest(h_amp_begin, 'CDF', [x_h_cdf(:), normal_CDF_h(:)]);
[h_KS_SSF_Ray, p_KS_SSF_Ray, KSstat_SSF_Ray, cv_KS_SSF_Ray] = kstest(h_amp_begin, 'CDF', [x_h_cdf(:), rayleigh_CDF_h_begin(:)]);
[h_KS_SSF_Rice, p_KS_SSF_Rice, KSstat_SSF_Rice, cv_KS_SSF_Rice] = kstest(h_amp_begin, 'CDF', [x_h_cdf(:), rician_CDF_h_begin(:)]);

fprintf('CDF normal distribution KS test results:\n');
fprintf('h=%d, p = %.6f, ksstat = %.6f, cv = %.6f\n', h_KS_LSF_Norm, p_KS_LSF_Norm, KSstat_LSF_Norm, cv_KS_LSF_Norm);
fprintf('CDF Rayleigh distribution KS test results:\n');
fprintf('h=%d, p = %.6f, ksstat = %.6f, cv = %.6f\n', h_KS_SSF_Ray, p_KS_SSF_Ray, KSstat_SSF_Ray, cv_KS_SSF_Ray);
fprintf('CDF Rice distribution KS test results:\n');
fprintf('h=%d, p = %.6f, ksstat = %.6f, cv = %.6f\n', h_KS_SSF_Rice, p_KS_SSF_Rice, KSstat_SSF_Rice, cv_KS_SSF_Rice);

% CDF of middle
figure(12);
cdfplot(h_amp_middle);
```

```
hold on;

x_h_cdf_mid = linspace(min(h_amp_middle), max(h_amp_middle),
length(h_amp_middle));
hat_sigma2_R_mid = 1 / (2 * length(h_amp_middle)) * sum(h_amp_middle.^2);
rayleigh_CDF_h_mid = 1 - exp(-x_h_cdf_mid.^2/(2 * hat_sigma2_R_mid));

rician_fit_mid = fitdist(h_amp_middle, 'Rician');
sigma_Rice_mid = rician_fit_mid.sigma;
upsilon_Rice_mid = rician_fit_mid.s;

rician_CDF_h_mid = 1 - marcumq(upsilon_Rice_mid/sigma_Rice_mid,
x_h_cdf_mid/sigma_Rice_mid);

plot(x_h_cdf_mid, rayleigh_CDF_h_mid, 'g-');
plot(x_h_cdf_mid, rician_CDF_h_mid, 'b-');

xlabel('Amplitude |h(t,\tau)|');
ylabel('CDF');
legend('Empirical CDF', 'Theoretical Rayleigh CDF', 'Theoretical Rice CDF');
title('CDF of the impulse response at middle');

% CDF of end
figure(13);
cdfplot(h_amp_end);
hold on;
hat_sigma2_R_end = 1 / (2 * length(h_amp_end)) * sum(h_amp_end.^2);
x_h_cdf_end = linspace(min(h_amp_end), max(h_amp_end),
length(h_amp_end));
rayleigh_CDF_h_end = 1 - exp(-x_h_cdf_end.^2/(2 * hat_sigma2_R_end));
```

```
rician_fit_end = fitdist(h_amp_end, 'Rician');
sigma_Rice_end = rician_fit_end.sigma;
upsilon_Rice_end = rician_fit_end.s;

rician_CDF_h_end = 1 - marcumq(upsilon_Rice_end/sigma_Rice_end,
x_h_cdf_end/sigma_Rice_end);

plot(x_h_cdf_end, rayleigh_CDF_h_end, 'g-');
plot(x_h_cdf_end, rician_CDF_h_end, 'b--');

xlabel('Amplitude |h(t,\tau)|');
ylabel('CDF');
legend('Empirical CDF', 'Theoretical Rayleigh CDF', 'Theoretical Rice CDF');
title('CDF of the impulse response at end');

% T1.5
% PDP book p111

%Doppler-variant impulse response
PDP = sum(abs(h_full).^2, 1) / size(h_full, 1);

figure(14);
plot(taus_full, 10*log10(PDP), 'b', 'LineWidth', 2);
xlabel('Delay (s)');
ylabel('PDP (dB)');
title('Power-Delay Profile (PDP)');
grid on;

% T1.6
```

```
P_m = sum(PDP);
T_m = sum(taus_full.*PDP) / P_m;
RMS = sqrt(sum(taus_full.^2.*PDP) / P_m - T_m^2);

fprintf('Mean delay: %.2f ns\n', T_m * 1e9);
fprintf('RMS Delay Spread S_\tau: %.2f ns\n', RMS * 1e9);

% T1.7
% Doppler-variant transfer function
% B(v,\tau)
% B = fft(h_full, [], 1) / sqrt(size(h_full, 1));
% P_B = sum(abs(B).^2, 1) / size(B, 2);
%
% figure(15);
% plot(10*log10(P_B), 'b', 'LineWidth', 2);
% xlabel('\upsilon (Hz)');
% ylabel('Doppler spectral density (dB)');
% title('Doppler spectral density');
%
% P_Bm = sum(P_B);
%
% % Time correlation
% time_corr = zeros(Nt*2-1, Nf);
% for f_idx = 1:Nf
%         time_corr(:, f_idx) = xcorr(Hcorrected(:, f_idx), 'coeff');
% end
%
% figure(12);
% x_pos = linspace(-Nt, Nt, Nt*2-1);
% plot(x_pos, mean(abs(time_corr), 2), 'b', 'LineWidth', 2);
```

```
% xlabel('Position (cm)');
% ylabel('Normalized Correlation');
% title('Time Correlation of H(t, f)');
% grid on;
%
% % Frequency correlation
% freq_corr = zeros(Nf*2-1, Nt);
% for t_idx = 1:Nt
%         freq_corr(:, t_idx) = xcorr(Hcorrected(t_idx, :), 'coeff');
% end
%
% figure(13);
%
% x_freq = linspace(-B_full/2, B_full/2, Nf*2-1);
% plot(x_freq, mean(abs(freq_corr), 2), 'r', 'LineWidth', 2);
% xlabel('Frequency offset (Hz)');
% ylabel('Normalized Correlation');
% title('Frequency Correlation of H(t, f)');
% grid on;
```

6.2 MIMO and Directional Aspects

```
clear; %Clear all variables in the workspace
close all; %Closes all figure windows
clc %Clear command window

%Load the data for Assignment 2
load('T_MIMO.mat');
```

```
Nf = 201;
frequencies = linspace(5.1e9, 5.3e9, Nf);
N_Tx = 8;
N_Rx = 8;

Rrr = zeros(N_Rx, N_Tx);

theta = linspace(0, pi, 361);
a = zeros(N_Rx, 1);
P_BF = zeros(Nf, size(theta, 2));
P_MVM = zeros(Nf, size(theta, 2));



for f_idx = 1 : Nf
    freq = frequencies(f_idx);
    lambda = 3e8 / freq;
    d = lambda / 2;

    H_f = T_MIMO(:, :, f_idx);

    Rrr = (H_f * H_f') / N_Tx;

    for theta_idx = 1:length(theta)
        a = exp(-1j * 2 * pi * d / lambda * cos(theta(theta_idx)) * (0:N_Rx-
1)');

        P_BF(f_idx, theta_idx) = (a' * Rrr * a) / (a' * a);

        Rrr_inv = Rrr \ eye(N_Rx);
        P_MVM(f_idx, theta_idx) = 1 / (a' * Rrr_inv * a);
```

```
        end

        % figure;
        % plot(theta, abs(P_BF(f_idx,:)), 'LineWidth',1.5);
        % plot(theta, abs(P_MVM(f_idx,:)), 'LineWidth',1.5);
end

P_BF_avg = mean(P_BF, 1);
P_MVM_avg = mean(P_MVM, 1);

P_BF_norm = abs(P_BF_avg) / max(abs(P_BF_avg));
P_MVM_norm = abs(P_MVM_avg) / max(abs(P_MVM_avg));

figure;
plot(rad2deg(theta), P_BF_norm, '--','LineWidth', 2);
hold on;
plot(rad2deg(theta), P_MVM_norm, '-', 'LineWidth', 2);
grid on;
xlabel('\theta (degrees)');
ylabel('Angle spectrum');
legend('P_{BF}(\theta)', 'P_{MVM}(\theta)');
hold off;
```